The Astrophysical Journal Letters, 954:L19 (11pp), 2023 September 1 https://doi.org/10.3847/2041-8213/aceefe

Discovery of Super-enriched Gas ∼1 Gyr after the Big Bang

Jianghao Huyan (呼延江豪)[1], Varsha P. Kulkarni[1], Suraj Poudel[2,3], Nicolas Tejos[2], Celine Péroux[4,5], and Sebastian Lopez[6]
[1] Department of Physics & Astronomy, University of South Carolina, Columbia, SC 29208, USA
[2] Instituto de Física, Pontificia Universidad Católica de Valparaíso, Casilla 4059, Valparaíso, Chile
[3] Department of Physics and Astronomy, Texas Christian University, Fort Worth, TX 76109, USA
[4] European Southern Observatory, Karl-Schwarzschildstrasse 2, D-85748 Garching bei München, Germany
[5] Aix Marseille Université, CNRS, LAM (Laboratoire d'Astrophysique de Marseille) UMR 7326, F-13388, Marseille, France
[6] Departamento de Astronomía, Universidad de Chile, Casilla 36-D, Santiago, Chile
Received 2023 June 7; revised 2023 July 28; accepted 2023 August 8; published 2023 August 31

Abstract

Abundances of chemical elements in the interstellar and circumgalactic media of high-redshift galaxies offer important constraints on the nucleosynthesis by early generations of stars. Damped Lyα absorbers (DLAs) in spectra of high-redshift background quasars are excellent sites for obtaining robust measurements of element abundances in distant galaxies. Past studies of DLAs at redshifts $z > 4$ have measured abundances of $\lesssim$0.01 solar. Here we report the discovery of a DLA at $z = 4.7372$ with an exceptionally high degree of chemical enrichment. We estimate the H I column density in this absorber to be $\log(N_{\rm H\,I}/{\rm cm}^{-2}) = 20.48 \pm 0.15$. Our analysis shows unusually high abundances of carbon and oxygen ([C/H] $= 0.88 \pm 0.17$, [O/H] $= 0.71 \pm 0.16$). Such a high level of enrichment a mere 1.2 Gyr after the Big Bang is surprising because of insufficient time for the required amount of star formation. To our knowledge, this is the first supersolar absorber found at $z > 4.5$. We find the abundances of Si and Mg to be [Si/H] $= -0.56^{+0.40}_{-0.35}$ and [Mg/H] $= 0.59^{+0.27}_{-0.50}$, confirming the metal-rich nature of this absorber. By contrast, Fe shows a much lower abundance ([Fe/H] $= -1.53^{+0.15}_{-0.15}$). We discuss implications of our results for galactic chemical evolution models. The metallicity of this absorber is higher than that of any other known DLA and is >2 orders of magnitude above predictions of chemical evolution models and the $N_{\rm H\,I}$-weighted mean metallicity from previous studies at $z > 4.5$. The relative abundances (e.g., [O/Fe] $= 2.29 \pm 0.05$, [C/Fe] $= 2.46 \pm 0.08$) are also highly unusual compared to predictions for enrichment by early stars.

Unified Astronomy Thesaurus concepts: Galaxies (573); Galaxy chemical evolution (580); Quasar absorption line spectroscopy (1317); Galactic abundances (2002); Circumgalactic medium (1879)

1. Introduction

The abundances of chemical elements in galaxies contain a fossil record of the star formation history of galaxies, since elements beyond helium ("metals") are produced essentially in stars, either in stellar cores or during supernova explosions. These products of stellar nucleosynthesis are shared with the interstellar medium (ISM) through stellar outflows and supernova ejecta. Subsequent generations of stars formed from this enriched ISM add more to the metal content of the ISM. Thus, as a galaxy evolves, its metallicity rises with time. The accretion and outflows of gas play key roles in the mixing of metals within and around the galaxy, since gas accretion brings in less-enriched gas, while gas outflows take away metal-enriched gas (e.g., Péroux et al. 2020). On a global scale, as star formation progresses in galaxies, the overall metal content increases with time. Models of chemical evolution thus predict that the global mean metallicity of galaxies was low at high redshifts and has been rising with cosmic time (e.g., Kulkarni et al. 2013; Maio & Tescari 2015; Yates et al. 2021). Observational measurements of metal abundances in galaxies at a variety of redshifts are required to test these predictions directly.

One way to determine metallicities of high-redshift galaxies is through measurements of nebular emission lines from their star-forming regions. However, this approach suffers from a number of uncertainties (e.g., Kewley & Ellison 2008), not to mention the rapidly increasing difficulty of detecting emission with increasing redshift. A powerful tool to circumvent this problem is to use absorption lines superposed by the galaxies in the spectra of bright background sources that lie at higher redshifts. The damped Lyα (DLA) and sub-DLA absorbers detected by means of their strong H I Lyα transitions in the spectra of background quasars (or gamma-ray burst afterglows) offer particularly robust ways to measure element abundances in distant galaxies. DLAs are defined as absorbers with H I column densities $N_{\rm H\,I} \geqslant 2 \times 10^{20}$ cm^{-2} and show strong radiation damping wings in the Lyα lines. Sub-DLAs are weaker, with $10^{19} \leqslant N_{\rm H\,I} < 2 \times 10^{20}$ cm^{-2}, but still show damping wings. The presence of these distinctive damping wings permits accurate determination of their H I column densities and, therefore, of their metal abundances, if combined with detections of optically thin metal absorption lines allowing accurate metal column density determinations.

A great deal of effort has been invested over the years on measuring element abundances in DLAs (e.g., Pettini et al. 1994; Prochaska et al. 2003; Kulkarni et al. 2005). Measurements for sub-DLAs are far less common, but have been growing with time (e.g., Kulkarni et al. 2007; Meiring et al. 2009; Som et al. 2013, 2015; Berg et al. 2021). While considerable scatter is seen in the metallicity–redshift relation for DLAs, sub-DLAs appear to

be more enriched than DLAs at $z < 2$ (e.g., Kulkarni et al. 2007; Meiring et al. 2009; Som et al. 2015). At $2 < z < 4.5$, the global DLA metallicity appears to drop by about 0.22 dex per unit redshift (e.g., Prochaska et al. 2003; Kulkarni et al. 2005, 2007; Meiring et al. 2009; Rafelski et al. 2012; Jorgenson et al. 2013; Som et al. 2013, 2015; Quiret et al. 2016).

The situation at $z > 4.5$ is not clear due to the lack of sufficiently large samples. A sudden drop in metallicity was reported in some past studies (e.g., Rafelski et al. 2012, 2014). But other studies (e.g., Poudel et al. 2018, 2020) find no evidence of such a drop and show that the claimed drop was probably a result of using refractory elements rather than volatile elements. A sudden drop would contradict predictions based on models of galaxy chemical evolution (e.g., Kulkarni et al. 2013; Maio & Tescari 2015; Yates et al. 2021). Regardless of the exact slope of the metallicity–redshift relation at $z > 4.5$, it is safe to say that most DLAs and sub-DLAs at $z > 4.5$ are found to be quite metal-poor, most with metallicities below $1/100$ solar, and essentially all below $1/10$ solar.

To better understand the metallicity evolution at $z > 4.5$, we are in the process of expanding the sample of element abundance measurements in high-z DLAs and sub-DLAs. Here we report the surprising discovery from this ongoing survey of a particularly interesting DLA at $z = 4.7372$ in the sight line to the quasar SDSS J002526.84-014532.5 that appears to be far more enriched than other known DLAs at comparable redshifts. This Letter is organized as follows: We describe our observations and data reduction in Section 2. Section 3 provides details of absorption-line measurements and determination of column densities. Section 4 discusses the determination of element abundances, a comparison with other DLAs from the literature and with predictions of galactic chemical evolution models, and other properties of the absorber. Finally, Section 5 summarizes our results.

2. Observations and Data Reduction

2.1. Observations

The quasar SDSS J002526.84-014532.5 ($z_{em} = 5.068$) was observed with the Magellan Clay telescope at the Las Campanas Observatory using the Magellan Inamori Kyocera Echelle (MIKE) spectrograph on UT 2021 September 5 and 6 (PID: CN2021B-57; PI: S. Poudel). MIKE offers simultaneous coverage of the orders on the red side (~4900–10000 Å) and the blue side (~3200–5000 Å) at spectral dispersions of ~0.05 Å and 0.02 Å, respectively. A 1″ slit was used, which yields a spectral resolving power of $R \approx 22{,}000$ on the red side and $R \approx 28{,}000$ on the blue side. In view of the faintness of our high-z quasar, binning by a factor of 2 was used in both the spatial and spectral directions to improve the signal-to-noise ratio (S/N). Thus the spectral resolution achieved was ≈11,000 on the red side and 14,000 on the blue side. Given the high redshift of our quasar, our primary interest lies in the spectra on the red side, as the blue side has very little flux owing to the extremely dense Lyα forest. An internal Th–Ar arc lamp was used as a comparison source for the purposes of wavelength calibration. An internal quartz lamp was used to obtain flat-field exposures. For obtaining good flat-field exposures that can correct for pixel-to-pixel sensitivity corrections, flats were also obtained with a diffuser slide inserted in the optical path. These "milky flats" allow the gaps between orders to be sufficiently illuminated (even at the edges) without sharing much light between the orders. Milky twilight flats were obtained using the bright O/B star HR6823 that has a high rotational velocity and thus broad spectral features that can be smoothed to obtain good flat-field images.

To supplement the MIKE observations, archival Very Large Telescope (VLT) X-shooter spectra of SDSS J002526.84-014532.5 (PID 098.A-0111, PI: M. Rafelski) were downloaded from the ESO Science Archive. The X-Shooter spectra have a considerably lower resolution than the MIKE spectra (with resolving power 8031 in the near-IR, 8935 in the VIS, and 5453 in the UV), but the wide wavelength coverage extending to 2478.9 nm provides access to longer-wavelength lines not covered in the MIKE spectra.

Table 1
Equivalent Width Measurements of Absorption-line Features for the $z = 4.7372$ DLA

λ_{obs} (Å)	ID	W_{rest} (mÅ)	log N_{AOD} (cm^{-2})
7470.8	O I λ 1302	683 ± 3	15.4 ± 0.04
8759.0	Si II λ1526	491 ± 3	14.9 ± 0.8
9228.0	Fe II λ 1608	205 ± 8	14.3 ± 0.02
16043.2	Mg II λ 2796	1556 ± 72	13.9 ± 0.7
16084.4	Mg II λ 2803	1290 ± 100	14.1 ± 0.2

2.2. Data Reduction

The MIKE data were reduced with a Python-based reduction pipeline, which uses the general process described by Kelson (2003). The pipeline includes the steps of bias subtraction, flat-fielding, extraction of one-dimensional spectra, wavelength calibration, coaddition of multiple exposures, and stitching of multiple orders.

The X-Shooter spectra downloaded from the ESO Science Archive were already reduced and extracted using the X-Shooter pipeline, which includes the steps of bias subtraction, flat-fielding, wavelength calibration, order merging, spectral extraction, sky subtraction, and flux calibration.

The extracted 1D spectra were continuum-fitted with a spline function using the program `Linetools` (Prochaska et al. 2017) and normalized by this continuum. The continuum-normalized spectra were searched for absorption lines at $z = 4.7372$, which is the redshift of the discovered DLA. The equivalent widths of all detected lines of H I and various metals were measured using `Linetools`. Table 1 lists these measurements.

3. Column Density Measurements

Approximate total column densities (integrated over all velocity components) of all ions with detected lines were first estimated using the apparent optical depth (AOD) method (Savage & Sembach 1996). More accurate column densities require careful multicomponent Voigt profile fitting and were determined using the Python code `Voigtfit` (Krogager 2018). Oscillator strengths were adopted from Cashman et al. (2017) where available, or from Morton (2003).

3.1. H I Line Fitting

Given the high redshift of the quasar, the Lyα forest is extremely dense. At such high redshifts, the continuum of the quasar becomes difficult to ascertain at wavelengths below the quasar's Lyα emission line. Continuum fitting was performed using the `Linetools` software. We fitted the H I line with the

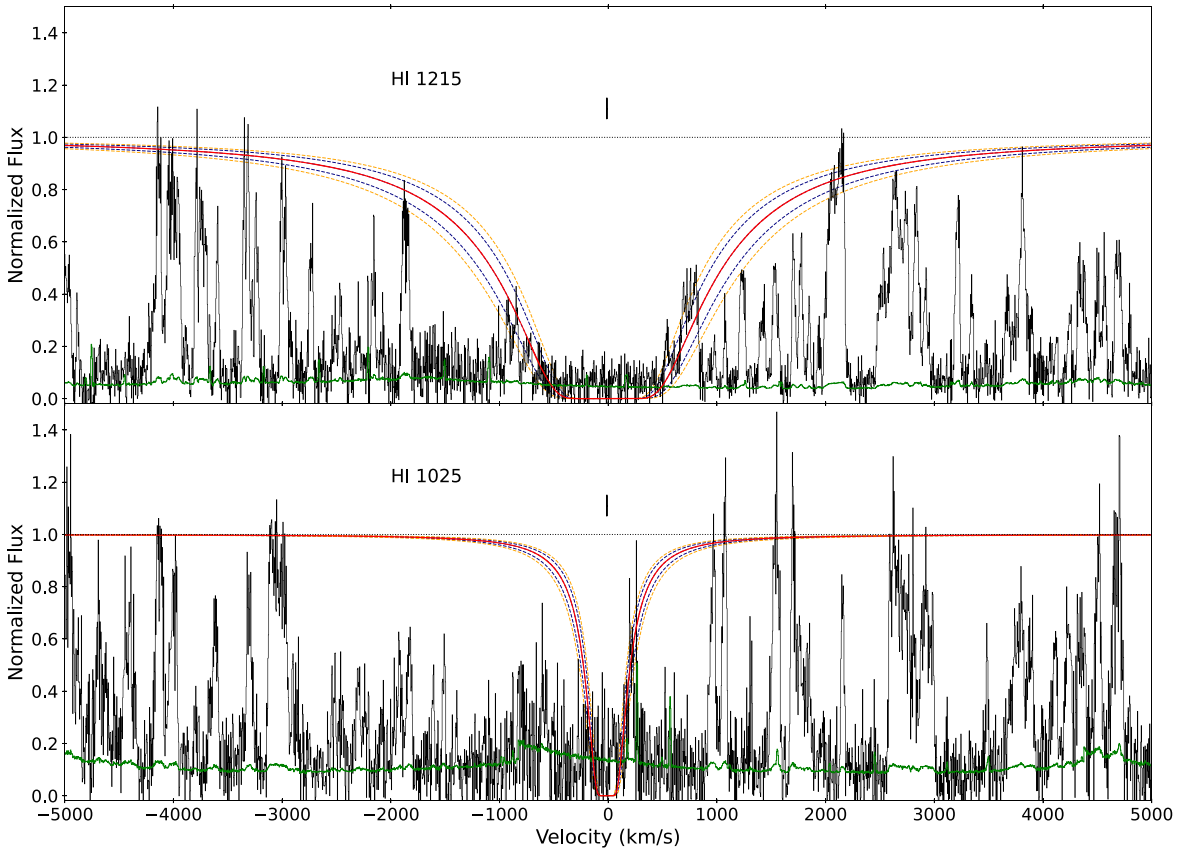

Figure 1. Normalized background quasar spectrum and Voigt profiles for the H I Lyα and Lyβ lines (top and bottom panels, respectively) for the $z = 4.7372$ absorber. The solid black vertical tick in each panel shows the H I component. The solid red and dashed navy blue curves show the Voigt profiles for log ($N_{\rm H\,I}$/cm^{-2}) = 20.48 ± 0.09. In addition, profiles for log $N_{\rm H\,I}$ values differing by ±0.15 dex (our adopted conservative uncertainties) are shown as dashed orange lines. The green curve at the bottom of each panel shows the 1σ flux error. The dotted horizontal lines show the putative continuum level used in the profiles shown with the red and orange curves.

`VoigtFit` code, paying attention to fitting the core, as seen in the Voigt profile fitting results shown in Figure 1 for the H I Lyα and Lyβ lines. We performed Voigt profile fitting using the "emcee" method. The Markov Chain Monte Carlo routine minimized the χ^2, which was calculated in the core region of the Lyα line at $z = 4.7372$ and other regions (including regions in the wings) not affected by the Lyα forest. The features unrelated to the Lyα absorption at $z = 4.7372$ were masked. The best-fitting H I column density was found to be log ($N_{\rm H\,I}$/cm^{-2}) = 20.48. We also repeated the fits after raising and lowering the continuum levels (a) by the 1σ flux uncertainties and (b) as judged visually. In all cases, we found the best-fitting H I column density to change by $\leqslant$±0.09 dex. To be conservative, given the difficulty in continuum determination, we adopt ±0.15 dex as the uncertainty in the H I column density.

3.2. Metal Line Fitting

Figure 2 shows the velocity plots for key metal ions, along with the results of Voigt profile fitting superposed. We note that in Figures 1 and 2, 0 km s^{-1} is defined with respect to the redshift of the strongest component in the metal lines (e.g., Si II, Fe II—see Figure 2), as is commonly done for DLAs, since the Lyα lines cannot give the velocity structure due to the damping wings. All available lines of each ion were fitted simultaneously. Comparison of multiple lines, where available, allowed us to perform deblending of the lines from unrelated lines of other absorption systems, or from telluric absorption.

One particularly complex spectral region is that containing the O I λ 1302, Si II λ 1304, and C II λ 1334 lines. This was examined carefully considering telluric lines as well as lines of other absorbers at different redshifts. Specifically, both O I λ 1302 and Si II λ 1304 are blended with C IV $\lambda\lambda$ 1548, 1550 doublets at $z \sim 3.8$, and C II λ 1334 is blended with telluric lines (∼7650–7660 Å). The emcee method implemented by the `lmfit` package in `VoigtFit` was used to fit the Voigt profiles of absorption features. The Si II λ 1526 and Fe II λ 1608 lines were fitted together, and the masked feature in Si II λ 1526 was ruled out by a comparison with Si II λ 1304 absorption features. Thereafter the Si II λ 1304 was fixed to resolve C IV doublets that are blended with both O I λ 1302 and Si II λ 1304. O I λ 1302 was then fitted together with O I λ 1355, after resolving all possible C IV lines that contaminate O I and Si II lines, and applying a similar component structure, except for redshifting the first component (component a) by 5 km s^{-1} and adding two weak extra components (labeled as g and h) to better align with the O I λ 1302 absorption features. O I λ 1355 is an extremely weak transition usually not detected in DLAs, but it can be detectable at very high O I column densities, which makes it useful as an additional constraint besides O I λ 1302 (i.e., to check that the O I column density is not too high). Figures 3(a)–(c) illustrate the careful deblending of O I λ 1302 and Si II λ 1304 from other contaminating lines. Figure 4 and the top panel of Figure 5 show the posterior

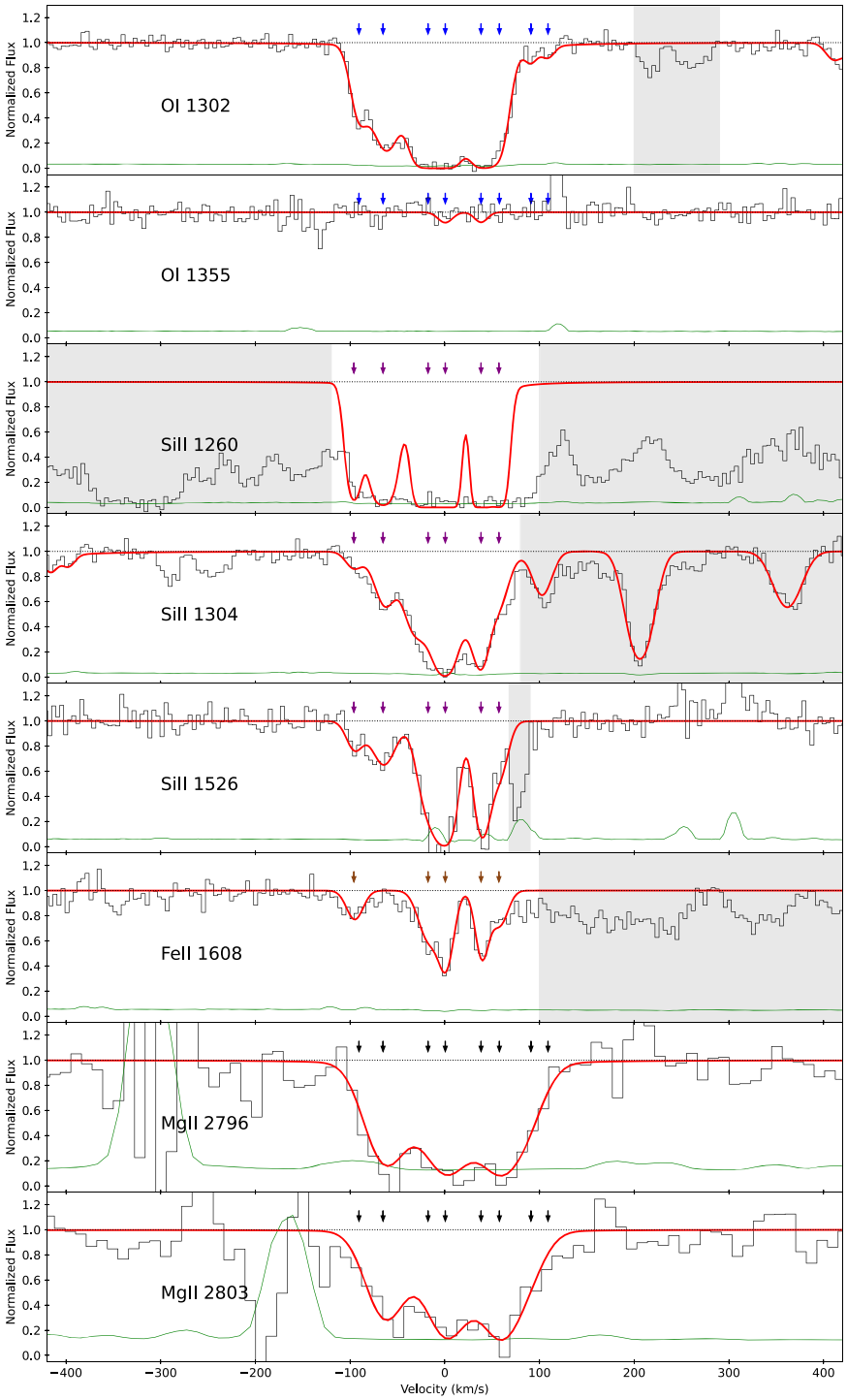

Figure 2. Velocity plots for several key metal absorption lines detected in the $z = 4.7372$ absorber in the spectra of SDSS J002526.84-014532.5 (O I λ 1302; Si II $\lambda\lambda\lambda$ 1260, 1304, 1526; and Fe II λ 1608 from MIKE; Mg II $\lambda\lambda$ 2796 2803 from VLT X-Shooter). Each panel shows the normalized flux in black and the 1σ noise level in green. The results of Voigt profile fitting are overplotted in red on the data; the arrows show the velocity components of the main ion, as listed in Table 2. The gray areas denote features unrelated to the absorption lines of interest. The Voigt profile fit near the Si II λ 1304 absorption line includes features of C IV $\lambda\lambda$ 1548, 1550 at lower redshifts $z \sim 3.8$; see Figure 3 for more details.

probability distributions of the various fitting parameters. The middle and bottom panels of Figure 5 show the absorption profiles for O I $\lambda\lambda$ 1302, 1355 for a range of column densities.

Observations of the star LTT 2415 were used as follows to estimate the extent of the telluric absorption blending in the C II λ 1334 line: (a) spectra of both the quasar J002526.84 −014532.5 and the standard star LTT2415 were normalized; (b) `specutils` (in Astropy) was used to resample the standard star spectrum to line up with the wavelength scale in the quasar spectrum; (c) an exponential correction was applied to the flux level of the standard star $f_{\rm corrected} = f^b$ where f is the normalized flux of the standard star, and $b = 1.1199$ is the ratio of the airmass values for the quasar and the standard star; and (d) the quasar spectrum was divided by the exponentially

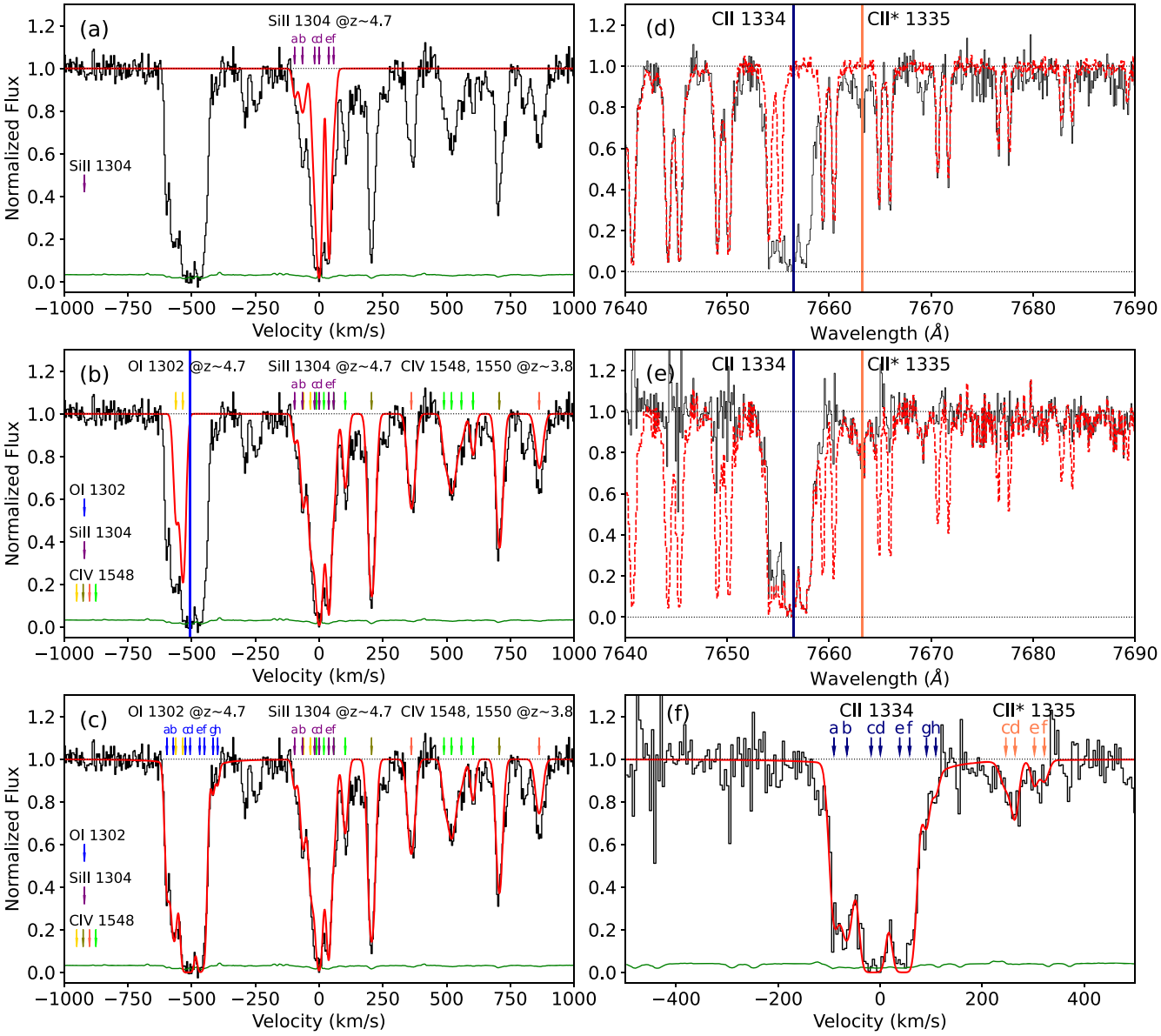

Figure 3. Left panels: the region near O I λ 1302 + Si II λ 1304 absorption lines in the $z = 4.7372$ absorber. (a) Voigt profile of Si II λ 1304, fixing parameters from Si II λ 1526. (b) Voigt profile of Si II λ 1304 with blending C IV $\lambda\lambda$ 1548, 1550 doublets at $z \sim 3.8$. The blue solid line indicates v = 0 km s^{-1} for O I λ 1302 absorption at $z = 4.7372$. (c) Voigt profile fitting results for O I λ 1302 after the blending C IV doublets are fitted. Right panels: the process of deblending C II λ 1334 from telluric features. (d) A comparison of spectra of the quasar (in solid black) and the standard star (in dashed red), and (e) a comparison of the quasar spectrum (in dashed red) and spectrum (in solid black) after normalization by the standard star spectrum for deblending telluric features. The blue and orange vertical lines show expected C II λ 1334 and C II* λ 1335 lines at $z = 4.7372$. (f) Fit of the remaining absorption after modeling the telluric lines. The arrows in panel (a)−(c) and (f) show the velocity components of main ions.

corrected spectrum of the standard star. Figures 3(d)–(f) illustrate these steps.

4. Results and Discussion

4.1. H I Lyα Flux Floor

As seen in Figure 1, the average flux level is not exactly zero in the center of the DLA absorption trough. We attribute this nonzero flux floor to two possible factors: (a) the light from the quasar host galaxy, or (b) the light from intervening galaxies close to the quasar sight line. The Hubble Space Telescope images of this field indeed show an unknown object separated by 0.″65 from the quasar sight line, which could be a potential source of light contamination to the DLA feature. We rule out the possibility that the foreground DLA on the sight line of the quasar J0025-0145 may be a case of partial coverage, as a nonzero flux floor is not seen in saturated metal lines.

4.2. Element Abundances

Table 1 lists the AOD column densities for the available metal ions in the $z = 4.7372$ absorber. Table 2 presents the results of the Voigt profile fitting for H I and the metal ions. For each ion detected, we list the column density, Doppler b parameter, and velocity with respect to $z = 4.7372$ for each of the individual velocity components, the total column density summed over all the velocity components, and the corresponding element abundance $[X/H] = \log N_X - \log N_H - \log (X/H)_\odot$, where the last term denotes the solar abundance (Asplund et al. 2009). Following common practice, we make no ionization correction for

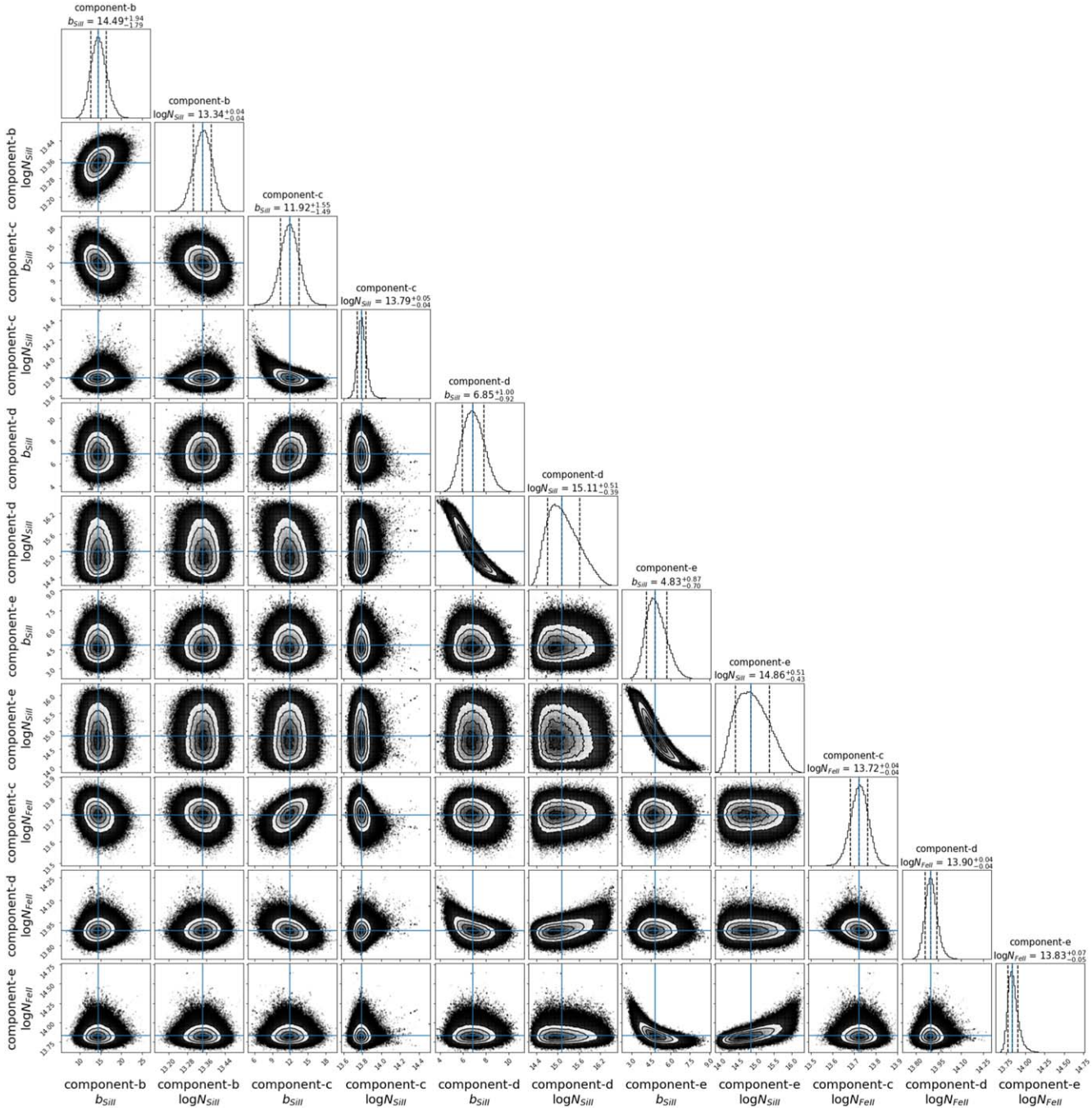

Figure 4. Posterior probability distribution of Doppler parameters b and the logarithm of column densities log N for dominant components of Si II λ 1526 and Fe II λ 1608. The median values are marked in solid blue lines, and 1σ intervals are marked in black dashed lines.

the DLA in view of its high H I column density, and assume a neutral phase with $N_{\rm H} = N_{\rm H\,I}$, and the column density of each metal to be that of its dominant ion.

We find that the $z = 4.7372$ absorber is highly enriched, with substantially supersolar C and O abundances $[{\rm C/H}] = 0.88^{+0.17}_{-0.17}$ and $[{\rm O/H}] = 0.71^{+0.16}_{-0.16}$. Given that C II λ 1334 may be saturated, the true C abundance could be even higher. To our knowledge, the metallicity of this DLA ([O/H]) is higher by a factor of >4 than that of other DLAs at *any* redshift in the literature (see, e.g., Rafelski et al. 2012; Som et al. 2015; Morrison et al. 2016; Quiret et al. 2016; and references therein). We stress that this conclusion is independent of any assumptions regarding the ionization level in the absorber, since O I has negligible ionization corrections (owing to the fact that the ionization potential of O I is very close to that of H I). The abundances of Mg ($[{\rm Mg/H}] = 0.59^{+0.27}_{-0.50}$) and Si ($[{\rm Si/H}] = -0.56^{+0.40}_{-0.35}$) are also very high compared to the abundances of Si or other α elements in other absorbers at comparable redshifts (e.g., Rafelski et al. 2012, 2014; Poudel et al. 2018, 2020). The abundance of Fe is much lower than the abundances of other elements in this DLA ($[{\rm Fe/H}] = -1.53^{+0.15}_{-0.15}$). This lower [Fe/H] and the lower abundance of Si relative to O suggest substantial dust depletion. Thus, we conclude that the $z = 4.7372$ absorber toward SDSS J002526.83-014532.5 arises in a highly enriched, dusty region.

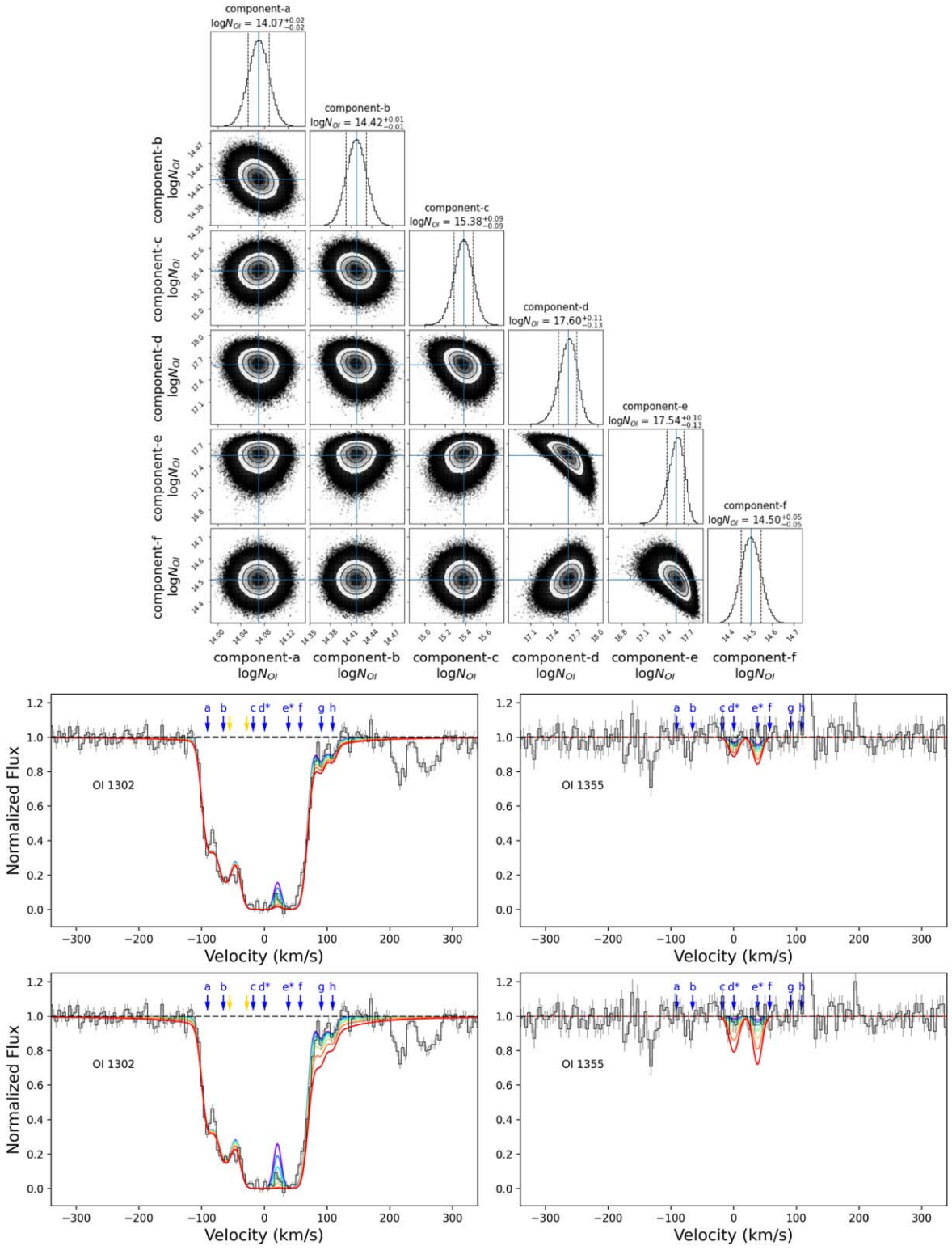

Figure 5. Top panel: posterior probability distribution of the logarithm of column densities log N for components of O I λ 1302. Middle and bottom panels: absorption profiles for O I $\lambda\lambda$ 1302, 1355 for a range of column densities, with the two dominant components (denoted with an asterisk) varied in increments of 0.1 dex over the ranges 17.14 to 17.74 and 17.27 to 17.87, and in increments of 0.2 dex over the ranges 16.84 to 18.04 and 16.97 to 18.17, respectively. In each panel, 1σ error bars are shown in gray. The yellow arrows indicate the C IV λ 1548 components blended with O I λ 1302 absorption.

We also note a surprising level of C enhancement, with $[C/Fe] = 2.46^{+0.08}_{-0.09}$ (i.e., a C/Fe ratio ~250 times the solar value) and $[C/O] = 0.17^{+0.09}_{-0.10}$. The C/O ratio may be somewhat different since some components of C II λ 1334 and O I λ 1302 may be saturated. In any case, if some of the C II components are saturated, the C/Fe ratio would be even higher, making this absorber even more carbon enhanced. To our knowledge, this is the first carbon-enhanced quasar absorber at $z > 4.5$. Carbon-enhanced metal-poor (CEMP) DLAs have previously been discovered at lower redshifts (e.g., Cooke et al. 2011, 2015, 2017) and are believed to be related

Table 2
Column Density and Abundance Measurements for the $z = 4.7372$ DLA[a]

Ion	Label	v (km s^{-1})	b (km s^{-1})	log N (cm^{-2})	log $N_{\rm total}$	[X/H]
O I	a	−90.6	8.66	$14.07^{+0.02}_{-0.02}$	$17.88^{+0.05}_{-0.04}$	$0.71^{+0.16}_{-0.16}$
	b	−65.2	14.47	$14.42^{+0.01}_{-0.01}$		
	c	−17.7	11.92	$15.38^{+0.09}_{-0.09}$		
	d	0.5	6.85	$17.60^{+0.11}_{-0.13}$		
	e	38.3	4.82	$17.54^{+0.10}_{-0.13}$		
	f	57.7	8.25	$14.50^{+0.05}_{-0.05}$		
	g	91.0	4.04	13.1		
	h	109.0	4.44	13.0		
Si II	a	−96.0	8.66	12.98	$15.43^{+0.37}_{-0.32}$	$-0.56^{+0.40}_{-0.35}$
	b	−65.2	$14.49^{+1.94}_{-1.79}$	$13.34^{+0.04}_{-0.04}$		
	c	−17.7	$11.92^{+1.55}_{-1.49}$	$13.79^{+0.05}_{-0.04}$		
	d	0.5	$6.85^{+1.00}_{-0.92}$	$15.11^{+0.51}_{-0.39}$		
	e	38.3	$4.83^{+0.87}_{-0.70}$	$14.86^{+0.51}_{-0.43}$		
	f	57.1	8.25	13.33		
C II	a	−90.6	8.66	$13.82^{+0.02}_{-0.02}$	$17.79^{+0.08}_{-0.08}$	$0.88^{+0.17}_{-0.17}$
	b	−65.2	14.47	$14.09^{+0.01}_{-0.01}$		
	c	−17.7	11.92	$15.56^{+0.06}_{-0.05}$		
	d	0.5	6.85	$14.84^{+0.24}_{-0.24}$		
	e	38.3	4.82	$17.79^{+0.08}_{-0.09}$		
	f	57.7	8.25	$14.64^{+0.14}_{-0.16}$		
	g	91.0	4.04	$12.98^{+0.08}_{-0.10}$		
	h	109.0	4.44	$12.60^{+0.10}_{-0.13}$		
Fe II	a	−96.0	8.66	13.35	$14.40^{+0.03}_{-0.02}$	$-1.53^{+0.15}_{-0.15}$
	c	−17.7	$11.92^{+1.94}_{-1.49}$	$13.72^{+0.04}_{-0.04}$		
	d	0.5	$6.85^{+1.55}_{-0.92}$	$13.90^{+0.04}_{-0.04}$		
	e	38.3	$4.83^{+1.00}_{-0.70}$	$13.83^{+0.07}_{-0.05}$		
	f	57.1	8.25	13.43		
Mg II	a	−90.6	8.66	$10.89^{+0.72}_{-0.62}$	$16.61^{+0.27}_{-0.50}$	$0.59^{+0.27}_{-0.50}$
	b	−65.2	14.47	$13.58^{+0.17}_{-0.15}$		
	c	−17.7	11.92	$12.57^{+0.63}_{-1.65}$		
	d	0.5	6.85	$16.46^{+0.34}_{-1.49}$		
	e	38.3	4.82	$12.45^{+2.16}_{-1.64}$		
	f	57.7	8.25	$15.42^{+0.80}_{-0.78}$		
	g	91.0	4.04	$12.77^{+0.73}_{-0.82}$		
	h	109.0	4.44	$11.06^{+0.79}_{-0.72}$		
C II*	c	−17.7	11.66	$12.93^{+0.08}_{-0.09}$	$13.53^{+0.03}_{-0.03}$	...
	d	0.5	6.85	$13.15^{+0.05}_{-0.05}$		
	e	38.3	4.82	$12.72^{+0.09}_{-0.11}$		
	f	57.7	8.25	$12.73^{+0.08}_{-0.09}$		

Note.
[a] Values without errors are fixed during the profile fitting analysis.

to nucleosynthesis by Population III stars. However, the CEMP DLAs are far less enriched than the C-enhanced metal-rich (CEMR) DLA we find toward SDSS J002526.83-014532.5. We note that the [C/H] and [C/Fe] levels in this DLA are comparable to the high values observed in some CH stars (e.g., Goswami et al. 2021). Finally, we note that O is also enhanced, with [O/H] $= 0.71 \pm 0.17$ and [O/Fe] $= 2.29 \pm 0.05$. If some of the O I 1302 components are saturated, this absorber would be even more oxygen enhanced with [O/Fe] $\geqslant 2.24$.

While the [C/O] ratio of $0.17^{+0.09}_{-0.10}$ in this DLA differs somewhat from that found in other absorbers at similar redshifts (e.g., ~ -0.3; see Bañados et al. 2019 and references therein), other relative abundances differ even more substantially. For example, the [C/Fe], [O/Fe], [C/Si], [O/Si], [Si/Fe], and [Mg/Fe] ratios in this DLA are 2.46, 2.29, 1.44, 1.27, 1.02, and 2.11, respectively, in sharp contrast to the typical values of ~ -0.1, 0.2, −0.3, 0.0, 0.4, and 0.3 found in other absorbers at $z \sim 5$ (e.g., Bañados et al. 2019 and references therein). The abundance patterns observed in the $z = 4.7372$ DLA toward SDSS J002526.83-014532.5 are also different from the predictions for Population III models (e.g., [O/Si] ~ -0.4 to 0.15 and [C/Fe] ~ -0.05 to 0.15 in

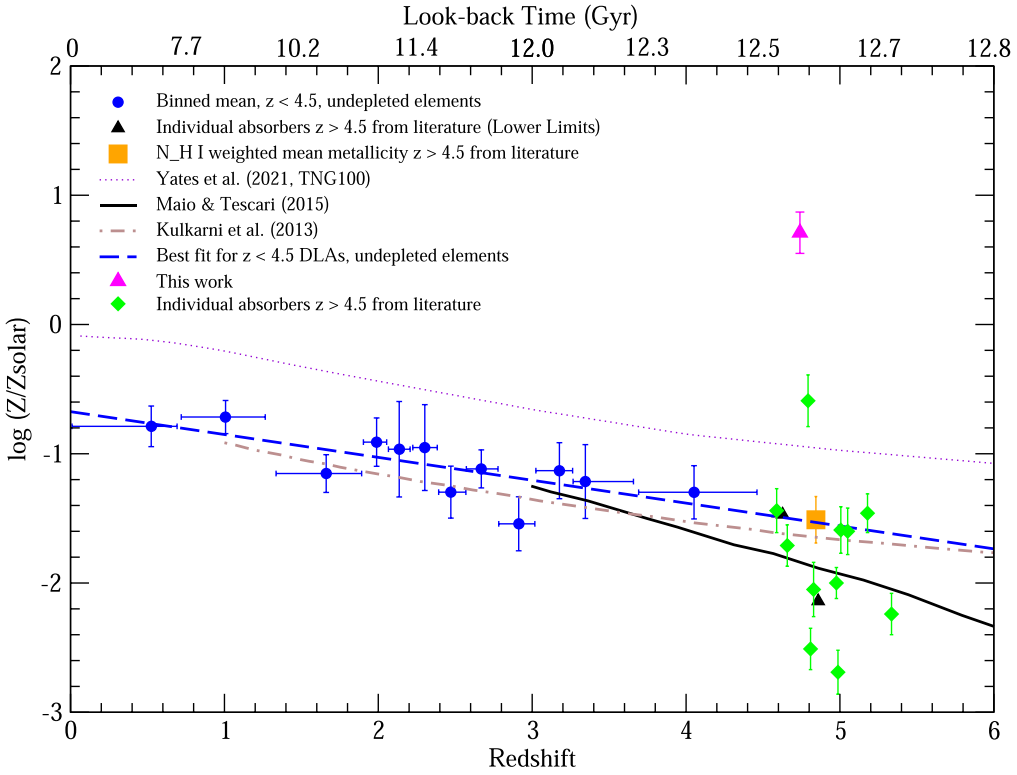

Figure 6. Comparison of the metallicity of the $z = 4.7372$ DLA with other DLAs at lower and similar redshifts and with models of chemical evolution. The metallicity of the $z = 4.7372$ DLA is over 2 orders of magnitude above that of other absorbers ($>9\sigma$ above the $N_{\rm H\ I}$-weighted mean metallicity at $z > 4.5$) and contrasts sharply with the low metallicities predicted by chemical evolution models.

the models of Kulkarni et al. 2014; [O/Si] ∼ 0–0.1, [C/O] ∼ −0.4 to −0.3, and [Si/Fe] ∼ 0.4 at $z \sim 5.5$ in the models of Ma et al. 2017).

The [Si/Fe] and [O/Fe] values for this DLA fall far beyond the ranges (∼0.1–0.8 and 0–1.1, respectively) simulated by Ma et al. (2017), but are consistent with an extrapolation of the trends seen at high [O/Fe] in their simulated trends (which would give [Si/Fe] ∼ 0.9 for [O/Fe] ∼ 2.2 for very massive (100–500 $M_\odot$) supernovae in Population II–dominated galaxies, and [Si/Fe] ∼ 0.6 for [O/Fe] ∼ 2.2 for massive supernovae (10–100 $M_\odot$) in Population III–dominated galaxies). The predicted [Si/O] ratio for $z \sim 5$ for the model of Kulkarni et al. (2013) using Salpeter initial mass functions (IMFs) with 100–260 $M_\odot$ for Population III and 0.1–100 $M_\odot$ for Population II stars is ∼0.2, in contrast to the value of −1.27 observed in the DLA toward SDSS J002526.83-014532.5.

4.3. Comparison with Other DLAs and Galaxy Evolution Models

Figure 6 shows a plot of metallicity versus redshift, showing the $z = 4.7372$ DLA presented here along with other DLAs from the literature (Rafelski et al. 2012, 2014; Poudel et al. 2018, 2020). The blue circles show the binned $N_{\rm H\ I}$-weighted mean metallicity versus redshift relation for DLAs at $z < 4.5$ (with each bin consisting of 16 or 17 DLAs). The dashed blue line shows the best fit for these $z < 4.5$ DLAs. The green diamonds denote the measurements for other individual $z > 4.5$ DLAs from the literature. It is clear that the $z = 4.7372$ DLA (shown as a purple triangle) is far more metal-rich than the typical metallicity of other DLAs at not just $z > 4.5$, but at any observed redshift. The golden square in Figure 6 shows the $N_{\rm H\ I}$-weighted mean metallicity of other DLAs at $z > 4.5$ from the literature (-1.51 ± 0.18) based on weakly depleted elements (Poudel et al. 2020). It is striking that the metallicity of the $z = 4.7372$ DLA in the sight line to SDSS J002526.84-014532.5 is >2.5 dex (over 300 times) higher than this mean value.

Also shown in Figure 6 are predictions from several models of chemical evolution (Kulkarni et al. 2013; Maio & Tescari 2015; Yates et al. 2021). All of these models clearly fall well below the very high O abundance and even the Si abundance of the $z = 4.7372$ DLA, both with and without the inclusion of Population III stars. It would be interesting to examine whether chemical evolution models with higher-mass Population III stars can lead to such extreme levels of enrichment at $z \sim 5$.

We note that the metallicity for the $z = 4.7372$ DLA is exceptionally high, and particularly unusual even for $z \sim 0$ star-forming galaxies. Pure core-collapse supernova ejecta are expected to have several times solar metallicity, as estimated by integrating supernova yields over a standard high-mass IMF. A metallicity of $\gtrsim$5 times solar can only be reached if a galaxy has weak or no outflows (so that all metals are retained in the ISM) and a low gas fraction, conditions not expected for galaxies at earlier cosmic epochs. On the other hand, reaching such high metallicities may be made easier with higher IMF-integrated supernova yields, e.g., with a top-heavy IMF.

Finally, we note that, since the spectroscopic observations of SDSS J002526.84-014532.5 probe only one sight line through the foreground galaxy, the gas properties along this sight line need not be representative of the whole galaxy. The $z = 4.7372$ DLA may probe an unusually metal-enriched region within the galaxy.

4.4. Dust Depletion Pattern

Based on the method of Jenkins (2009; as explained in Quiret et al. 2016), one can estimate the depletion strength F_*

and the depletion-corrected metallicity from the measured gas-phase abundances using the relation $[X_{gas}/H] = B_X + A_X(F_* - Z_X)$. If the parameters A_X, B_X, and Z_X for the Milky Way (MW) ISM are adopted for the $z = 4.7372$ DLA in the sight line to SDSS J002526.84-014532.5, the depletion strength is estimated to be $F_* = 1.04$ including the five observed elements (C, O, Si, Fe, and Mg), and 1.26 excluding Mg (given the larger uncertainties in the Mg II column density). The depletion strength in this DLA thus appears to be much larger than that in other DLAs at $z > 4.5$ (-1.13 to -0.81; Poudel et al. 2020) and the typical value in lower-redshift DLAs (-0.70; Quiret et al. 2016). The large F_* value in the $z = 4.7372$ DLA toward J002526.84-014532 is, in fact, similar to that in the cool disk gas in the MW ($F_* \sim 0.90$), suggesting the presence of significant dust depletion in this DLA. The corresponding dust-corrected metallicity in this sight line inferred from the Jenkins (2009) method is 1.11 dex including Mg and 1.07 dex excluding Mg, suggesting a highly metal-rich composition.

The very low Fe abundance relative to the α elements O, Mg, and Si may be partly a nucleosynthetic effect, since the Fe/α abundance ratio is affected by both dust depletion and the age of the stellar population. This is because Fe is predominantly enriched by Type Ia supernovae requiring much longer timescales ($\sim$0.3–1 Gyr) than the timescales for core-collapse supernovae ($\sim$10 Myr) that dominate the production of α elements. However, this nucleosynthetic difference (α/Fe enrichment) is expected to be only $\sim$0.4 dex, not enough to explain the very low abundance of Fe relative to O, Si, and Mg without dust depletion. If the gas-phase Fe abundance is raised by 0.4 dex to account for this effect, and the parameters A_X, B_X, and Z_X for the MW ISM are adopted, the depletion strength estimate would be $F_* = 0.87$ including Mg and $F_* = 1.05$ excluding Mg, and the corresponding estimates of the dust-corrected metallicity would be 1.06 dex and 1.02 dex, respectively.

On the other hand, the dust properties in this DLA may not be similar to those in the MW ISM. Indeed, the vastly different abundances of Si, Mg, and Fe relative to O are surprising, given that in the MW and lower-redshift DLAs, the depletion of Mg is only slightly higher than or similar to that of Si and lower than that of Fe (see, e.g., Jenkins 2009; De Cia et al. 2016). The difference between the abundances of Si and Mg is tentative ($\sim 2\sigma$, given the uncertainties in the column densities of both Si II and Mg II). The Mg II lines lie in a noisy region of the X-shooter spectrum. On the other hand, if the Mg II lines are saturated, the true Mg abundance could be higher.

If higher spectral resolution and higher-S/N observations can resolve any saturation issues in the X-Shooter data and continue to indicate very different abundances of Si, Mg, and Fe relative to O, that may indicate that the dust grain composition in this high-z galaxy is different from that in the MW ISM. The MW ISM shows roughly similar depletions of Mg and Si (e.g., Jenkins 2009) and similar amounts of Fe and Mg in the dust phase suggestive of a composition of an olivine ($Mg_{2x}Fe_{2(1-x)}$ SiO_4) or pyroxene ($Mg_xFe_{1-x}SiO_3$) type of silicate with $x \sim 0.5$ (i.e., $MgFeSiO_4$ or $MgFeSi_2O_6$; see, e.g., Min et al. 2007; Draine 2011; Hensley & Draine 2021). Other studies (e.g., Mattsson et al. 2019) suggest that interstellar silicates in the MW as well as DLAs may be a mixture of both iron-poor ($x \sim 0$) and iron-rich ($x \sim 1$) minerals in the olivine and pyroxene families. If the silicate dust in the $z = 4.7372$ DLA is dominated more by iron-rich olivines closer to fayalite (Fe_2SiO_4) than to $MgFeSiO_4$, or iron-rich pyroxenes closer to ferrosilite ($FeSiO_3$) than to $MgFeSi_2O_6$, one would expect Mg to be substantially less depleted from the gas phase than Fe. Differences in dust grain composition (especially in the ratio of silicate to carbonaceous dust) can lead to substantial differences in extinction curve shapes (e.g., Asano et al. 2014); thus significant differences in dust grain composition in distant galaxies can potentially have implications for the accuracy of dust extinction corrections for high-z galaxies.

4.5. Electron Density

The electron density (n_e) can be constrained from the ratio of the column densities of C II and C II* under the assumption that collisional excitation and spontaneous radiative deexcitation are in equilibrium $N_{C\,II*}/N_{C\,II} = n_e C_{12}(T)/A_{12}$, where the collision rate coefficient is a function of temperature $C_{12}(T) = [8.63 \times 10^{-6}\Omega_{12}/(g_l T^{0.5})]\exp(-E_{12}/kT)$, and the C II* spontaneous radiative deexcitation rate $A_{21} = 2.29 \times 10^{-6}$ s^{-1}. In the collision rate coefficient $C_{12}(T)$, $g_1 = 2$, $E_{12} = 1.31 \times 10^{-14}$ erg, and Ω_{12} depends on temperature. At $T \sim 7000$ K, $\Omega_{12} = 2.81$ given $C_{12}(7000\,\mathrm{K}) = 1.43 \times 10^{-7}$. Since C II is saturated, $N_{C\,II*}/N_{C\,II} \leqslant 5.37 \times 10^{-5}$, implying an upper limit on the electron density $n_e \leqslant 8.60 \times 10^{-4}$ cm^{-3}. At $T \sim 500$ K, $\Omega_{12} = 1.82$, giving $C_{12}(500\,\mathrm{K}) = 2.90 \times 10^{-7}$, and an electron density limit of $n_e \leqslant 4.24 \times 10^{-4}$ cm^{-3}. This is $\gtrsim$5–10 times lower than the median n_e of 0.0044 ± 0.0028 cm^{-3} in the general DLA population (Neeleman et al. 2015), possibly suggesting less active "current" star formation caused by gas consumption and/or feedback from the past higher level of star formation that enriched this galaxy.

5. Summary

We have discovered highly enriched gas at $z = 4.7372$ by means of its extremely strong metal absorption features in a DLA system. The O and C abundances in the absorbing region are $\sim$5 times solar and $\sim$8 times solar, respectively, while the Si abundance is about 1/3 solar. These high levels of enrichment contrast sharply with the N(H I)-weighted metallicity of other DLAs at comparable redshifts, and also with the available galactic chemical evolution models with and without Population III stars. The absorber at $z = 4.7372$ also appears to be dusty, as judged from the depletion of Si, Fe, and Mg. The wide differences between the depletion levels of Si, Fe, and Mg suggest that the dust grains in this distant galaxy may have a different chemical composition compared to the interstellar dust in the MW. Future observations of SDSS J002526.83-014532.5 would be highly useful to shed more light on the galaxy in its foreground presumably associated with the DLA at $z = 4.7372$. Higher spectral resolution observations would help to determine more accurate element abundances and confirm whether the dust depletion pattern indeed differs from that in the MW. Given the high level of dust depletion, this sight line may also be rich in molecules. While the H_2 Lyman and Werner bands are inaccessible due to the dense Lyα forest, it would be interesting to search for other molecular species with future millimeter/submillimeter observations. An accurate determination of the molecular gas and dust content in this DLA would allow a more robust determination of the physical properties and chemical enrichment of its ISM. Finally, spatially resolved spectroscopy would enable identification of

the galaxy associated with the DLA, and mapping of the distributions of metallicity, gas kinematics, and star formation rate in and around this intriguing galaxy at $z \sim 5$.

Acknowledgments

We thank the anonymous referee for constructive suggestions that have helped to improve this paper. J.H. and V.P.K. acknowledge partial support from the National Science Foundation grants AST/2007538 and AST/2009811 (PI: Kulkarni). V.P.K. gratefully acknowledges additional support from NASA grant 80NSSC20K0887 (PI: Kulkarni). S.P. would like to express gratitude for the support received from the ESO-Chile joint committee grant. S.L. acknowledges support by FONDECYT grant 1231187. This Letter incorporates data collected through the program CN2021B-57 (PI: Poudel) using the Magellan/MIKE telescope, situated at Las Campanas Observatory, Chile. We thank the Las Campanas Observatory staff for assistance in conducting the observations.

Facilities: Magellan:Clay, VLT:Kueyen.

Software: Astropy (The Astropy Collaboration et al. 2013, 2018), VoigtFit (Krogager 2018), Linetools (Prochaska et al. 2017).

ORCID iDs

Jianghao Huyan (呼延江豪) https://orcid.org/0009-0004-0648-9529
Varsha P. Kulkarni https://orcid.org/0000-0002-2587-2847
Suraj Poudel https://orcid.org/0000-0003-0536-3081
Nicolas Tejos https://orcid.org/0000-0002-1883-4252
Celine Péroux https://orcid.org/0000-0002-4288-599X
Sebastian Lopez https://orcid.org/0000-0003-0389-0902

References

Asano, R. S., Takeuchi, T. T., Hirashita, H., & Nozawa, T. 2014, MNRAS, 440, 134
Asplund, M., Grevesse, N., Sauval, A. J., & Scott, P. 2009, ARA&A, 47, 481
Bañados, E., Rauch, M., Decarli, R., et al. 2019, ApJ, 885, 59
Berg, T. A. M., Fumagalli, M., D'Odorico, V., et al. 2021, MNRAS, 502, 4009
Cashman, F. H., Kulkarni, V. P., Kisielius, R., Ferland, G. J., & Bogdanovich, P. 2017, ApJS, 230, 8
Cooke, R., Pettini, M., Steidel, C. C., et al. 2011, MNRAS, 412, 1047
Cooke, R. J., Pettini, M., & Jorgenson, R. A. 2015, ApJ, 800, 12
Cooke, R. J., Pettini, M., & Steidel, C. C. 2017, MNRAS, 467, 802
De Cia, A., Ledoux, C., Mattsson, L., et al. 2016, A&A, 596, A97
Draine, B. T. 2011, Physics of the Interstellar and Intergalactic Medium (Princeton, NJ: Princeton Univ. Press)
Goswami, P. P., Rathour, R. S., & Goswami, A. 2021, A&A, 649, A49
Hensley, B. S., & Draine, B. T. 2021, ApJ, 906, 73
Jenkins, E. B. 2009, ApJ, 700, 1299
Jorgenson, R. A., Murphy, M. T., & Thompson, R. 2013, MNRAS, 435, 482
Kelson, D. D. 2003, PASP, 115, 688
Kewley, L. J., & Ellison, S. L. 2008, ApJ, 681, 1183
Krogager, J.-K. 2018, arXiv:1803.01187
Kulkarni, G., Hennawi, J. F., Rollinde, E., et al. 2014, ApJ, 787, 64
Kulkarni, G., Rollinde, E., Hennawi, J. F., et al. 2013, ApJ, 772, 93
Kulkarni, V. P., Fall, S. M., Lauroesch, J. T., et al. 2005, ApJ, 618, 68
Kulkarni, V. P., Khare, P., Péroux, C., et al. 2007, ApJ, 661, 88
Ma, Q., Maio, U., Ciardi, B., et al. 2017, MNRAS, 472, 3532
Maio, U., & Tescari, E. 2015, MNRAS, 453, 3798
Mattsson, L., De Cia, A., Andersen, A. C., & Petitjean, P. 2019, A&A, 624, A103
Meiring, J. D., Lauroesch, J. T., Kulkarni, V. P., et al. 2009, MNRAS, 397, 2037
Min, M., Waters, L. B. F. M., de Koeter, A., et al. 2007, A&A, 462, 667
Morrison, S., Kulkarni, V. P., Som, D., et al. 2016, ApJ, 830, 158
Morton, D. C. 2003, ApJS, 149, 205
Neeleman, M., Prochaska, J. X., & Wolfe, A. M. 2015, ApJ, 800, 7
Péroux, C., Nelson, D., van de Voort, F., et al. 2020, MNRAS, 499, 2462
Pettini, M., Smith, L. J., Hunstead, R. W., et al. 1994, ApJ, 426, 79
Poudel, S., Kulkarni, V. P., Cashman, F. H., et al. 2020, MNRAS, 491, 1008
Poudel, S., Kulkarni, V. P., Morrison, S., et al. 2018, MNRAS, 473, 3559
Prochaska, J. X., Gawiser, E., Wolfe, A. M., et al. 2003, ApJL, 595, L9
Prochaska, J. X., Tejos, N., Crighton, N., et al. 2017, Linetools/Linetools: Third Minor Release, v0.3, Zenodo, doi:10.5281/zenodo.1036773
Quiret, S., Péroux, C., Zafar, T., et al. 2016, MNRAS, 458, 4074
Rafelski, M., Neeleman, M., Fumagalli, M., et al. 2014, ApJL, 782, L29
Rafelski, M., Wolfe, A. M., Prochaska, J. X., et al. 2012, ApJ, 755, 89
Savage, B. D., & Sembach, K. R. 1996, ARA&A, 34, 279
Som, D., Kulkarni, V. P., Meiring, J., et al. 2013, MNRAS, 435, 1469
Som, D., Kulkarni, V. P., Meiring, J., et al. 2015, ApJ, 806, 25
The Astropy Collaboration, et al. 2013, A&A, 558, A33
The Astropy Collaboration, et al. 2018, AJ, 156, 123A
Yates, R. M., Péroux, C., & Nelson, D. 2021, MNRAS, 508, 3535